



Characterization of a high-pressure flame facility using high-speed chemiluminescence and OH LIF imaging

Will Swain¹ · Yejun Wang¹ · Pradeep Parajuli¹ · Matthew Hay¹ · Ahmad Saylam² · Thomas Dreier² · Christof Schulz² · Waruna Kulatilaka¹

Received: 10 November 2022 / Revised: 9 February 2023 / Accepted: 21 February 2023 / Published online: 18 March 2023
© The Author(s), under exclusive licence to Springer-Verlag GmbH Germany, part of Springer Nature 2023

Abstract

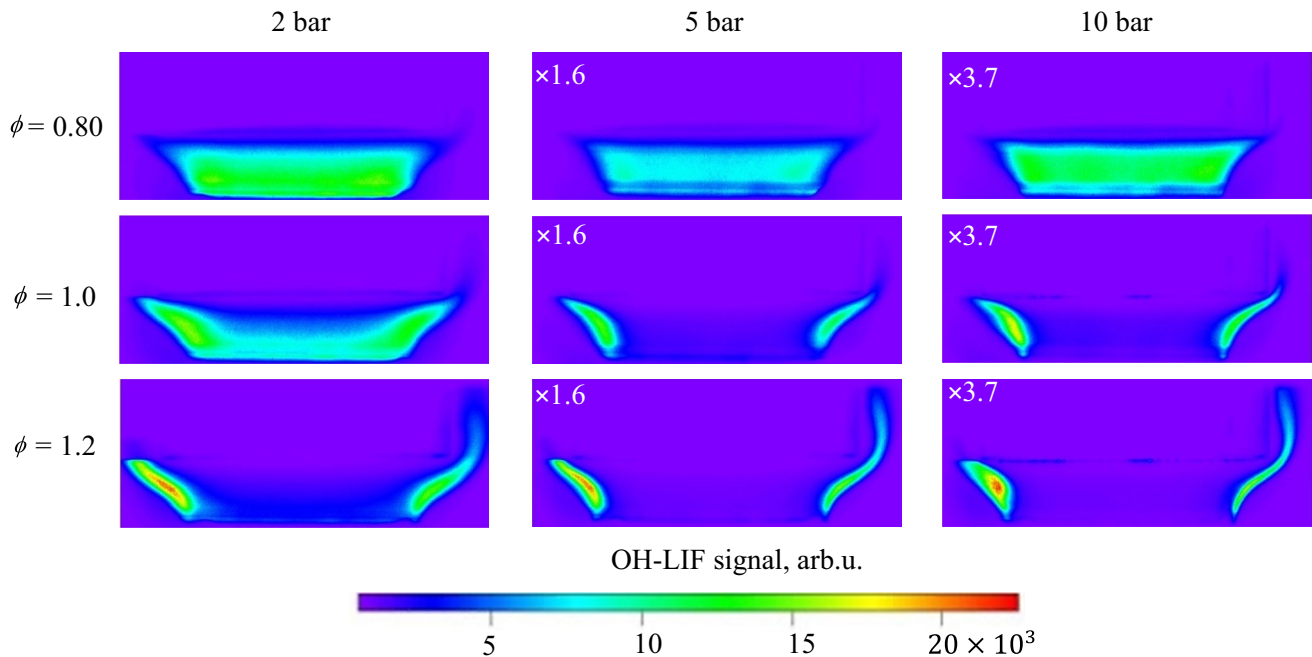
The combustor and turbine inlet pressures of modern aviation and power-generation gas turbine engines can vary between 30 and 50 bar. Innovative diagnostic methods are needed to understand the complex thermo-physical processes taking place under these conditions. Non-intrusive, spatially, and temporally resolved optical and laser diagnostic methods such as chemiluminescence and laser-induced fluorescence imaging (LIF) can be used to gain insights into flame stability, heat release, and pollutant formation processes. In this work, a laboratory-scale, optically accessible, high-pressure burner facility operating on premixed CH₄/air flames is developed and characterized using kHz-rate hydroxyl and methylidyne chemiluminescence imaging, OH-LIF imaging, and two-color OH-LIF thermometry. For the latter two measurements, the flames were stabilized up to 10 bar using a stainless-steel disk mounted above the burner surface. Approximately 10-ns duration Nd:YAG laser pulses at 283.305 nm were used to excite the Q₁(7) rotational line of the A²Σ⁺ ← X²Π (1,0) band of the OH radical, followed by fluorescence detection from the A ← X (1,1) & (0,0) bands. A linear dependence of the OH-LIF signal on the laser energy was observed. An increase in pressure from 1 to 10 bar showed a nonlinear decay of the OH-LIF signal. While quenching corrections accounted for a fraction of the signal loss, additional mechanisms, such as laser beam absorption and signal trapping, need to be considered for complete signal quantification. The measured excitation spectrum compared well with the LIFBASE model predictions. The flame equivalence ratio scans at different pressures agreed with the Cantera equilibrium flame code calculations. 2D OH-concentration distributions and two-color OH-LIF temperature maps agreed qualitatively with flame simulations performed using the ANSYS Fluent software package. This well-characterized burner facility provides a testbed for combustion and soot formation studies and investigates the role of minor species at elevated pressures at gas-turbine-relevant flame conditions.

✉ Waruna Kulatilaka
waruna.kulatilaka@tamu.edu

¹ J. Mike Walker '66 Department of Mechanical Engineering,
Texas A&M University, College Station, TX 77843, USA

² EMPI, Institute for Energy and Materials Processes –
Reactive Fluids, University of Duisburg-Essen, Duisburg,
Germany

Graphical Abstract



1 Introduction

Gas turbine engines are an integral part of the modern world. These engines are widely used in the aerospace, power generation, and oil & gas industries and are critical to everyday human activities. Efficiency, emissions, and stable operation are key areas of concern that can be improved drastically through combustion research. Higher inlet temperatures, advanced materials, and cooling methods all can contribute to an increase in efficiency (Mom and Jansohn 2013). A better understanding of the combustion process can reduce pollutant emissions (including soot formation) into our atmosphere. Even a minor increase in thermal efficiency or decrease in pollutant formation results in direct economic benefits via reduced fuel costs and better compliance with increasing emission standards. Gas turbine engines typically operate in the 30–50 bar pressure range. Yet, most combustion studies reported in the literature are focused on atmospheric or low-pressure flames. While this data are useful for fundamental understanding, it cannot be directly extended to higher-pressure operational conditions. The need for experimental tools suitable for realistic engine scenarios is often solved by introducing well-characterized high-pressure burners suitable for advanced optical measurements and modeling.

High-pressure burners are a unique experimental tool used to simulate combustion processes inside realistic engines and other combustion devices. The basic concept is to place a burner—typically producing a flat laminar flame—inside of a large pressure vessel with sufficient mechanical and thermal characteristics while producing ample optical access for emission and laser-based diagnostics. A key challenge in these burners is generating a stable flame and ensuring proper thermal management. Non-intrusive laser diagnostics are currently the preferred method to obtain thermochemistry data required for validating complex flame models. Several institutions have developed high-pressure burner facilities and implemented optical diagnostics (Leschowski et al. 2015; Frank et al. 1999; Atakan et al. 1997; Kim et al. 2019; Matynia et al. 2012; Bessler et al. 2002a, b; Attal-Trétout et al. 1990; Kohse-Höinghaus et al. 1990; Hofmann et al. 2003). Besides a fundamental understanding of combustion under such conditions, the focus of these studies had been centered on increasing combustion efficiency and decreasing emissions. Although the results have been promising, much work needs to be performed to implement recently developed advanced laser diagnostics to elevated pressure conditions (Wang et al. 2019a, Kulatilaka et al. 2007, Kuehner et al. 2008). However, before testing and implementing advanced diagnostics, the high-pressure flames must

be well characterized. For this paper, three well-established diagnostic techniques, chemiluminescence imaging of electronically excited hydroxyl (OH*) and methylidyne (CH*) radicals (Parajuli et al. 2021), hydroxyl radical laser-induced fluorescence (OH-LIF) imaging (Kulatilaka et al. 2011), and two-color OH-LIF thermometry (Wang et al. 2019b) are used to characterize a high-pressure flame facility suitable for testing novel laser diagnostics (Parajuli et al. 2022; Wang et al. 2019b; Jain et al. 2021)) as well as soot nucleation studies (Wang et al. 2021).

Chemiluminescence (CL) refers to spontaneous light emissions from chemically produced excited species to lower electronic states. Chemical species are electronically excited by chemical reactions. In particular, OH* and CH* radical detection schemes provide useful insight into reaction zone conditions, flame oscillations, and local equivalence ratios. OH* is a good marker of the reaction zone, while CH* represents the flame front (Tobias et al. 2019; Zhao et al. 2018; Nori and Seitzman 2009; Arndt et al. 2015; Kojima et al. 2005). Chemiluminescence monitoring requires minimal additional hardware and hence, can be readily extended to high-pressure combustion experiments. The main limitation of the chemiluminescence technique is that the signal acquired is volume averaged. Therefore, localized flame features may be averaged out, and results may not provide a complete depiction of the flame structure. However, it can be readily implemented to reveal flame oscillations and can be extended to kilohertz (kHz) or even megahertz (MHz) data rates using high-speed cameras and image intensifiers. Several laboratories have applied tomographic reconstruction and thus spatially resolved CL imaging techniques to overcome this issue (Mohri et al. 2017; Cai et al. 2013).

On the other hand, OH-LIF is a spatially and temporally resolved laser diagnostic technique that involves exciting specific rovibrational transitions between two electronic states of the hydroxyl radical with a tunable laser. As the molecule deactivates back to its lower energy state, resulting fluorescence emission can be imaged from the excited planar region providing a two-dimensional snapshot of the flame. This technique has been proven to be able to detect minor species concentration, mixture fraction, temperature, pressure, and velocity (Boxx et al. 2015).

OH-LIF involves two main stages, the first being the molecule absorbing the laser energy and reaching a higher energy state, followed by the relaxation of that molecule, causing the emission of a photon. Pressure broadening will occur at the first stage as the targeted linewidth of the excitation will become significantly broader due to pressure effects (Atakan et al. 1997; Matynia et al. 2012; Kohse-Höinghaus et al. 1990). Quenching effects are the main issue during the second stage and the underlying reason behind why accurate measurements are difficult to obtain at high pressure. Collisional quenching is the dominant mechanism

when transitioning into higher pressures, as noted by Atakan et al. (1997) and Carter and Laurendeau (1994). The basic premise is that when the molecules are excited to an elevated state, some of the energy does not release as an emitted photon; instead, the excited molecules collide with other species, and their energy is released during the collision as thermal energy instead of fluorescence. The pressure increase increases the number of molecular collisions; therefore, collisional quenching will increase significantly. Quenching is the main reason the OH-LIF signal is considerably weaker at elevated pressure, even though theoretically, the signal should be increasing to reflect the increase in the number density of the OH radical.

OH-LIF thermometry measurement techniques were employed to determine the temperature profile of the flame at various equivalence ratios and pressures. Temperature distributions can provide critical information about the combustion process, including key insights into the efficiency and pollutant formation of a specific combustor (Roy et al. 2002). Thermocouple probes can provide this temperature data, but probing the flame may disturb the natural reactive flow during combustion, and mechanical probes can be damaged or act catalytically in harsh environments. Therefore, OH-LIF thermometry, a non-invasive measurement technique, is preferable as it does not disturb the flame (Wang et al. 2019b). Previous studies have demonstrated the effectiveness of various OH-LIF thermometry schemes (Kohse-Höinghaus et al. 1990; Dulin et al. 2021; Seitzman and Hanson 1993; Devillers et al. 2008); in this study, OH-LIF thermometry was performed based on the two-excitation intensity-ratio technique using the $Q_1(5)$ line and the $Q_1(14)$ line excited at 282.750 and 286.456 nm, respectively. The $Q_1(5)$ to $Q_1(14)$ LIF signal ratio was compared with a fifth-order polynomial fit determined by Wang and co-workers (Wang et al. 2019b) to determine the temperature. A line-peak LIF technique was utilized for this comparison.

Thermocouples are widely employed to measure gas temperature in flames. However, in general, measured values must be corrected regarding heat losses by radiation or conduction using several approaches (Hindasageri et al. 2013; Krishnan et al. 2015; Kaskan 1957). Since for such corrections to be meaningful, the environmental conditions at the measurement position need to be known with sufficient accuracy. Therefore, some authors use flame simulations to provide this information or publish the uncorrected data (Do et al. 2021; Betrancourt et al. 2022).

This work aims to characterize the new high-pressure burner facility at Texas A&M University utilizing chemiluminescence, OH-LIF, and OH-thermometry measurements. The scope of this paper includes the experimental and simulation details, processes, results, and conclusions drawn from the process. Details of the burner geometry and the experimental setups for the different diagnostic techniques

are outlined. Chemiluminescence data is then presented to compare the spatial distributions of the OH ground state (via LIF). Moreover, numerical results obtained from the 2D simulations under development are compared to the experimentally obtained OH contours to compare experimental and numerical results. Thermocouple measurements of gas-phase temperature are compared with the results from OH-LIF thermometry. The simulations are conducted in the CFD package ANSYS Fluent using a partially premixed combustion model. The limitations of high-pressure combustion experiments are discussed upon deviations from the theoretical calculations.

2 Experimental method and CFD model

2.1 High-pressure burner facility

Measurements were conducted inside of an optically accessible laboratory scale high-pressure burner with the capability of reaching pressures up to 50 bar, Fig. 1. Within a collaborative project between our two research laboratories, there are currently two identical burners in use, one of them at Texas A&M University and the other at the University of Duisburg-Essen. Both burners were copies from an initial version developed at Châtillon, France, where Attal-Trétout et al. (1990) and Kohse-Höinghaus et al. (1990) recorded CARS and OH-LIF thermometry measurements. The pressure vessel surrounding the burner is constructed of 316 stainless steel with four 14-mm thick quartz optical windows (45 mm diameter, with a clear aperture of 28 mm) located symmetrically around the central axis allowing for laser penetration and optical access to the flame inside. The burner

located inside the pressure vessel consists of a 20-mm diameter central porous bronze plate delivering a premixed flow of methane and air and a 13.5-mm thick bronze ring with a co-flow of air to straighten the premixed flame to increase stability. The air co-flow also ensures any excess fuel was burnt before reaching the windows or the exhaust valve. A nitrogen guard flow was also utilized to convectively cool the vessel and prevent thermal stress on the windows due to increased temperatures. Figure 1 shows the CAD model highlighting some of the critical elements in both the outer view and a cross-sectional view and an image of the high-pressure burner in its current configuration.

Pressure control of the burner during the tests was implemented by regulating the exhaust flow through a pneumatically driven research control valve and a National Instruments data acquisition system. An piezoelectric pressure transducer inside the burner monitored the pressure and relayed a signal to a DAQ (National Instruments USB-6001 DAQ). The DAQ then delivered a signal to the PID loop, which adjusted the signal air pressure to the control valve to either increase or decrease the exhaust valve orifice. Cooling was accomplished through the combined efforts of both the previously mentioned guard flow and copper water cooling lines encircling the midsection of the burner body, as well as a cooling coil embedded inside the porous bronze plate of the burner itself and a cooling head at the top of the burner to cool the exhaust gases. The cooling system successfully maintained temperatures to ensure the safe operation of the burner. Lastly, a stabilization disk was added to help minimize the oscillations of the flame during combustion. Experiments were conducted at 1–10 bar with flame conditions ranging from lean $\phi = 0.7$ to rich $\phi = 1.3$. The pressure range was limited to 1–10 bar due to the mass flow

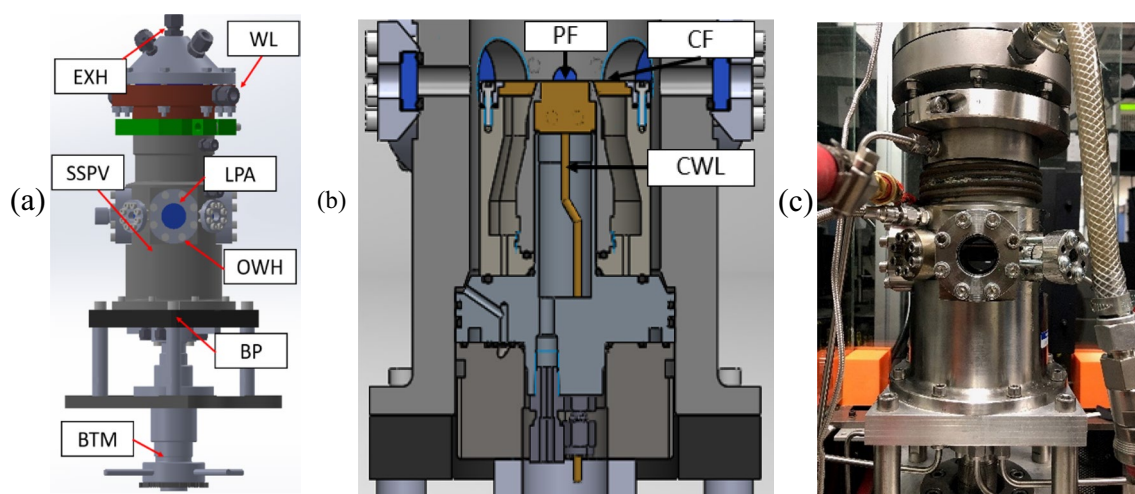


Fig. 1 High-pressure burner images **a** SolidWorks model: EXH: exhaust, WL: water lines, LPA: laser penetration area, BP: baseplate, OWH: outside window holder, BTM: burner translation mechanism,

SSPV: stainless steel pressure vessel **b** Burner cross-sectional view: PF: premixed flow, CF: co-flow, CWL: cooling water line **c** Photograph of the assembled burner

controllers available at the time. Additionally, this work is an initial characterization of the High-Pressure Burner Facility at Texas A&M, modifications are being made to increase the operating pressure. The methane flow varied from 0.163 slm (standard liters per minute) at the lean low-pressure condition to 1.21 slm at the rich high-pressure condition. The airflow varied from 2.1 to 9.53 slm. A combination of MKS mass flow controllers and Matheson flowmeters were used to introduce gases into the system. The MKS mass flow controllers regulated the premixed CH_4 and air, and the Matheson flowmeters regulated the air co-flow and the N_2 guard flow. The MKS mass flow controllers used had an accuracy of $\pm 1\%$ of the set point value while the Matheson flowmeters had an accuracy of $\pm 5\%$ of the full-scale value. The flow-rates at the changing pressures are documented in Table 1.

2.2 Experimental procedure

The chemiluminescence experiments were conducted using a Photron Fastcam SA-Z camera paired with a LaVision high-speed intensified relay optics (HS-IRO) module shown in Fig. 2. During chemiluminescence testing, three different emissions were recorded using optical bandpass filters in front of the HS-IRO module. CH^* was recorded using a 434 ± 8.5 -nm filter, OH^* was recorded using a 315 ± 7.5 -nm filter, and the broadband chemiluminescence was recorded with no filter. All tests were sampled at a 1-kHz repetition rate, the HS-IRO gate was set to 0.5 ms, and the intensifier gain was varied for each filter being used but remained constant during the pressure and equivalence ratio scans. The preliminary testing determined appropriate gain values of 55% for CH^* , 45% for OH^* , and 40% for broadband emissions. The spatial dispersion of the imaging configuration was determined to be 19 pixels per mm using a calibration target. The resulting chemiluminescence images were processed by integrating the signal across the flame for each frame.

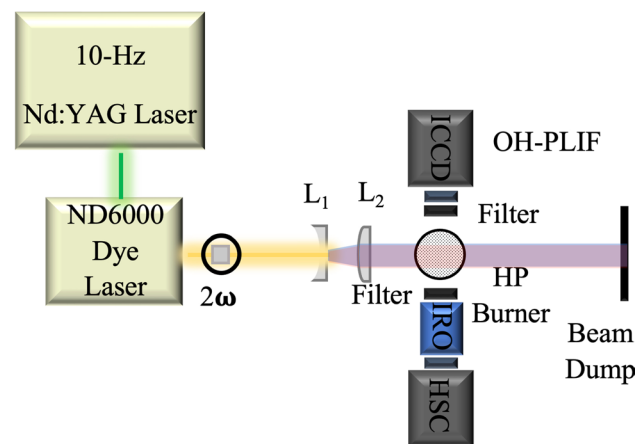


Fig. 2 Experimental setup for OH-LIF high-pressure imaging measurements

For OH-LIF imaging studies, a nanosecond-pulse Nd:YAG laser (Continuum, Model: Powerlite 8000) operating at 1064 nm. The frequency-doubled 1064-nm beam generated 532-nm pulses that were used to pump a tunable dye laser (TDL) (Continuum, ND6000). The dye laser was filled with rhodamine-590 dye mixed in methanol to generate a 566.6-nm beam. The output beam was frequency-doubled using a BBO crystal to obtain 283.305 nm in vacuum for $Q_1(7)$ excitation of the $\text{OH } A^2\Sigma^+ \leftarrow X^2\Pi(1,0)$ band. The typical linewidth of the frequency-doubled dye laser is 0.1 cm^{-1} , according to the manufacturer's specifications. The UV beam was then redirected using several 45° dielectric mirrors to the probe region and converted to a thin laser sheet using a combination of a cylindrical lens ($f = -75 \text{ mm}$) and a spherical lens ($f = +750 \text{ mm}$); this lens combination produced a laser sheet approximately $160 \mu\text{m}$ in thickness. The UV laser beam was fixed at a diameter of 5 mm prior to the cylindrical and spherical lenses. To improve image quality, only the nearly uniform central portion of the UV laser was used. An intensified CCD camera (ICCD) (Princeton

Table 1 Gas flow rate

Pressure (bar)	$\phi = 0.8$		$\phi = 1.0$		$\phi = 1.2$		Co-flow (slm)
	CH_4 (slm)	Air (slm)	CH_4 (slm)	Air (slm)	CH_4 (slm)	Air (slm)	
1	0.184	2.2	0.226	2.16	0.266	2.12	5.17
2	0.369	4.41	0.453	4.32	0.532	4.21	10.3
3	0.474	5.66	0.581	5.56	0.684	5.45	15.5
4	0.421	5.03	0.515	4.94	0.607	4.85	20.7
5	0.525	6.29	0.643	6.17	0.758	6.06	25.8
6	0.471	5.66	0.578	5.56	0.681	5.45	31.0
7	0.55	6.61	0.674	6.48	0.794	6.36	36.2
8	0.627	7.55	0.769	7.41	0.905	7.27	41.4
9	0.704	8.5	0.864	8.33	1.02	8.18	46.5
10	0.781	9.44	0.958	9.26	1.13	9.09	51.7

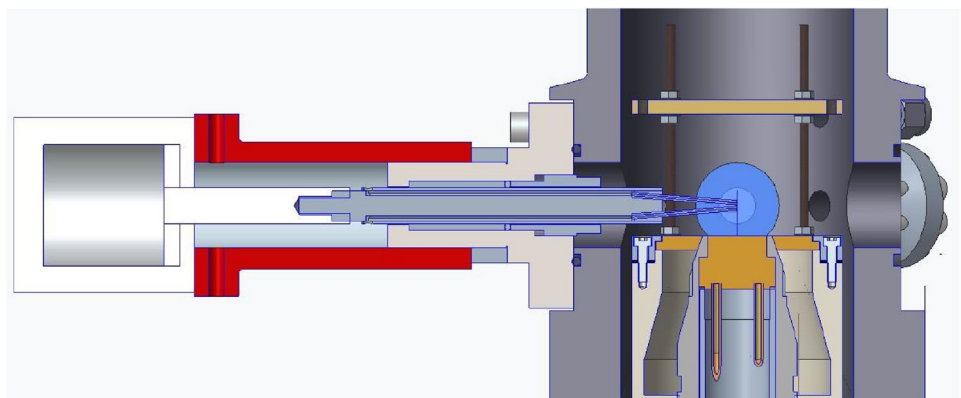
Instruments, PI-MAX4) fitted with a +100-mm focal-length $f/2$ UV camera lens (Bernard Halle) was placed perpendicularly to the beam propagation to capture the fluorescence signal from the A←X (1,1) & (0,0) bands. A filter was placed on the lens of the camera to specifically collect the targeted 308 nm fluorescence and block out unwanted interferences. The complete laser and imaging systems are shown in Fig. 2. The images taken had resolutions of 1024×1024 pixels and were time-averaged for 150 shots, the spatial dispersion was found to be 22 pixels/mm. Thermometry measurements were taken utilizing this same setup but by exciting the $Q_1(5)$ line at 282.750 nm and the $Q_1(14)$ line at 286.456 nm and calculating the ratio between the two for comparison with a calibration function (Wang et al. 2019b).

Thermocouple (TC) measurements were performed in a twin burner located at the University of Duisburg-Essen. A pneumatically driven TC sampler, similar in design by Leschowski et al. (2014) for soot sampling and shown in Fig. 3, was quickly inserted and retracted into the flame at the centerline position for a few seconds until thermal equilibration. This method avoids TC damage by too long overheating and possible soot deposition for rich flame conditions. Soot deposits on the TC junction will increase heat losses depending on increased emissivity values. The thermocouple was type B (Pt 6% Rh/Pt 30% Rh) with a bead diameter of 0.2 mm. Measurements at different height above the burner (HAB) positions were realized by moving the burner to fixed sampler positions. Radial profiles at a fixed HAB were accomplished by varying the distance between the threaded sampler cylinder (red part in Fig. 3) and the window flange (light gray part in Fig. 3).

Measured thermocouple (TC) temperature values were corrected for radiation loss using three approaches from the literature and subsequently forming average values. One is the correction calculated from Eq. 5 in Kaskan (1957)

$$T_g = T_{tc} + \frac{1.25\epsilon_{tc}\sigma T_w^4 d^{3/4}}{\lambda} \left(\frac{\eta}{\rho v}\right)^{1/4} \quad (1)$$

Fig. 3 Sketch of the pneumatically driven thermocouple sampler connected to one of the window flanges of the burner



In this equation, T_g is the corrected gas temperature, T_{tc} the TC bead temperature, ϵ_{tc} the emissivity of the bead, T_w the assumed wall temperature, d the bead diameter, λ , η , and ρ are heat conduction, viscosity and density, respectively, of the surrounding gas, and v is the local gas velocity. The temperature-dependent emissivity was taken from the expression given by Shaddix (1999) for an S-type thermocouple. The thermophysical gas properties were calculated from suitable functions fitted to data tabulated in the NIST Chemistry WebBook (2023), SRD 69. Assumed gas compositions were either pure nitrogen, or calculated from by Gaseq 2023 for a product gas equilibrium mixture at the measured TC temperature for methane combustion at the respective equivalence ratios in this work. Finally, the local gas velocity was calculated from Ansys Chemkin-Pro 2023 with a chemical kinetics mechanism of methane combustion (GRI Mech).

In another approach, the expression.

$$T_g = T_{tc} + \epsilon_{tc}\sigma(T_{tc}^4 - T_w^4) \frac{d}{kNu} \quad (2)$$

given in Shaddix (2017) was used, with the thermal conductivity, k , of the gas mixture and two different correlation expressions for the Nusselt number, Nu :

$$Nu = 0.42Pr^{0.2} + 0.57Pr^{1/3}Re_d^{0.5} \quad (3)$$

In this expression, the Prandtl number and the Reynolds number (with respect to the wire diameter), Pr and Re_d , respectively, are given by Kramers (1946) (and cited as Eq. (14) in Shaddix (1999)). The second Nu correlation (also cited in Shaddix (1999) as Eq. (13)) is the one by Collis and Williams (1959):

$$Nu = (0.24 + 0.56Re_d^{0.45}) \left(\frac{T_m}{T_\infty}\right)^{0.17} \quad (4)$$

for flows across cylinders. Here, T_m is the so-called film temperature, i.e., the mean of the thermocouple, and freestream temperature T_∞ .

2.3 Computational model

Combustion in the high-pressure burner facility was simulated with ANSYS Fluent, using a partially premixed combustion model. Figure 4 shows the model of the computational domain used for the simulations. A 2D axisymmetric solver was selected, allowing the simulations to be conducted only in half of the domain. The premixed CH_4/air enters through a 10-mm inlet, and the co-flow enters through a 13.5-mm inlet based on the burner dimensions. The domain extends to 40 mm in the x -direction and to 38 mm in the y -direction. The commonly used k-epsilon standard model was adopted as the turbulence model. Partially premixed combustion was selected, and the GRI-Mech 2023 2.11 kinetics mechanism with 49 species and 279 reactions was implemented. Because of the small domain size constrained by the dimension of the burner enclosure, we were able to discretize the model into uniformly fine grids at every location. The grids were generated with a face meshing tool, each element being quadrilateral in shape and 100 μm in size. The element size was significantly smaller than the reaction layer thickness of approximately 1 mm, based on the full-width-at-half-maximum of the radial OH signal profile. A bias factor could be applied for the larger domain to minimize the grid size in the region of interest. The mesh statistics created are highlighted in Table 2.

Once the mesh is generated, the boundary conditions were provided in the setup section. The inlet flow mixtures

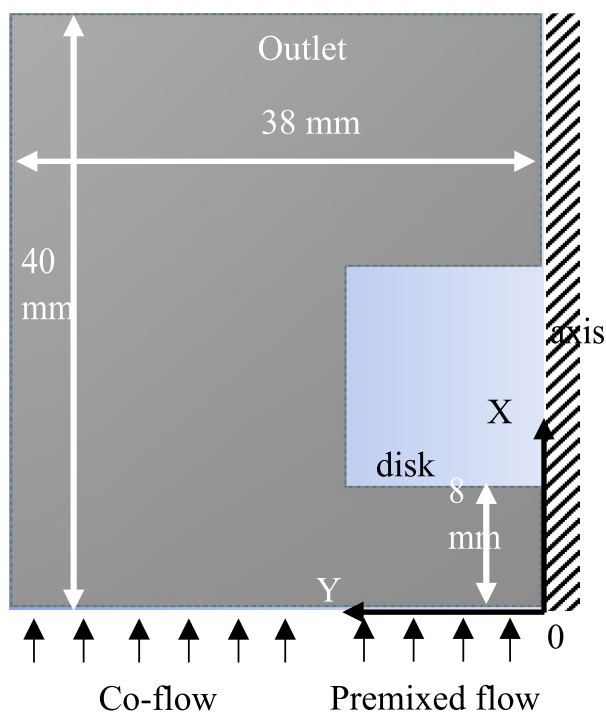


Fig. 4 Computational domain

Table 2 Mesh statistics

Statistics	Values
Nodes	119,021
Elements	118,150
Minimum orthogonal quality	0.999
Maximum orthogonal skewness	5.952×10^{-7}
Maximum aspect ratio	1.417

were fed at ambient temperature conditions in terms of mass flow rate to match the flow rates used in the experiments. All flows are set normal to the boundary. Because of axial symmetry, an axis condition was provided to the right edge of the domain to perform 2D simulations to save computational time. A wall boundary condition is provided to the left edge of the domain, which corresponds to the wall of the pressure vessel. The outlet at the top was defined as a pressure outlet. A wall boundary condition of estimated equilibrium temperature 1000 K is provided to the stagnation disk surface facing the inlet, which is close to what has been measured with a thermocouple inserted from the back side of the disk. A semi-implicit method for pressure-linked equations (SIMPLE) algorithm was used as a numerical procedure to solve the Navier–Stokes equations. It is often preferred for steady-state problems because it can converge solutions quickly. A second-order upwind setting was set for all solvers (momentum, turbulent kinetic energy, energy, and progress variable) to increase the accuracy of the solution. In addition, a convergence criterion for each residual was set to 1×10^{-4} except for the energy for which it was set to 1×10^{-6} to obtain better convergence. The domain was initialized as a Hybrid initialization. The number of iterations was set to 1×10^4 and the simulation was left for convergence.

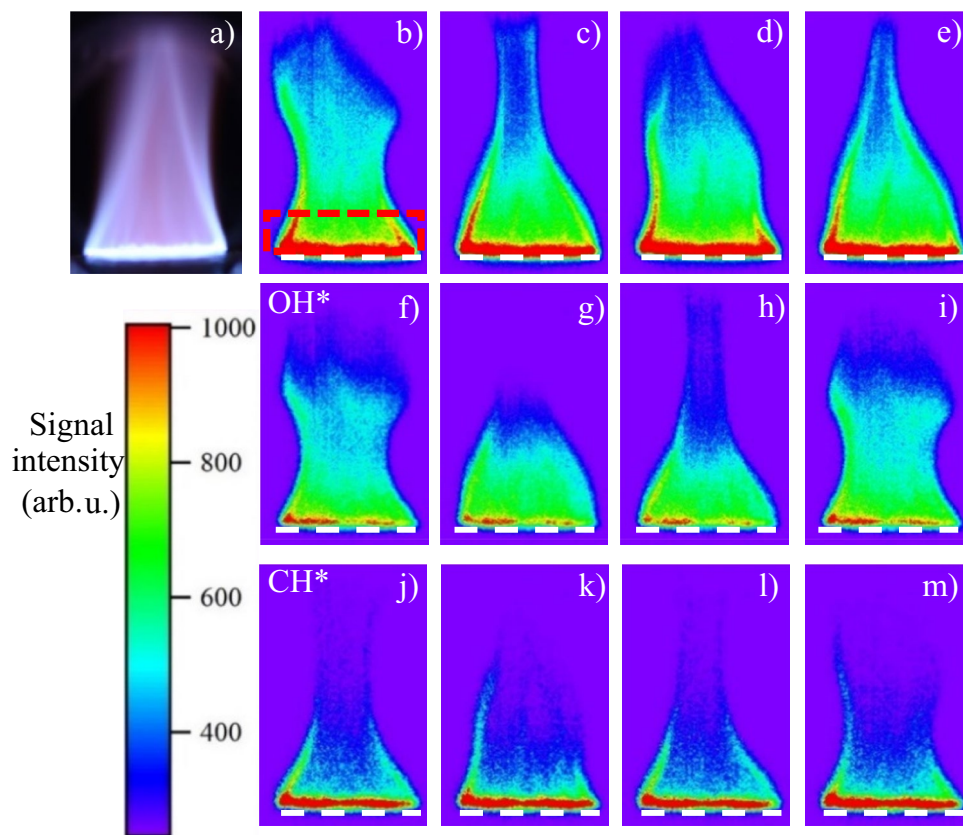
3 Results

3.1 High-speed chemiluminescence studies

Chemiluminescence images were taken to analyze and characterize the high-pressure flames. The first pressure and equivalence ratio scans showed that the flame was unstable in the current burner configuration. Figure 5 shows oscillations in the broadband, OH^* , and CH^* chemiluminescence images of the $\phi = 1.2$ flame at 8 bar. The first image in each series (row) is the flame at the maximum integrated signal; the second image is the minimum integrated signal, followed by another maximum and minimum image. Oscillations similar to these were seen across the entire pressure and equivalence ratio range.

Flame oscillations are undesirable for flame diagnostic techniques; therefore, the unstable flame was stabilized

Fig. 5 Photo of flame measurements **a**, false-color images of broadband chemiluminescence **b–e**, OH* chemiluminescence **f–i**, and CH* chemiluminescence **j–m** at 8 bar $\phi = 1.2$ showing flame oscillations of the unstable flame. The red dashed line indicates the signal integration area (6.2 mm \times 19.2 mm)



by positioning an axisymmetric stainless-steel disk 8 mm above the burner surface. The disk is held in place by two stainless-steel rods mounted to two auxiliary ports on the pressure vessel, allowing full optical access to the stable flame. Figure 6 depicts the sample single shot images

(b, e), 1000 single-shot-averaged images (averaged during post-processing) (c, f), and averaged images from an ICCD camera (averaged on the chip) (d, g) of OH* (top row) and CH* (bottom row) chemiluminescence for the constrained flame ($p = 8$ bar, $\phi = 1.2$) shown in the inset

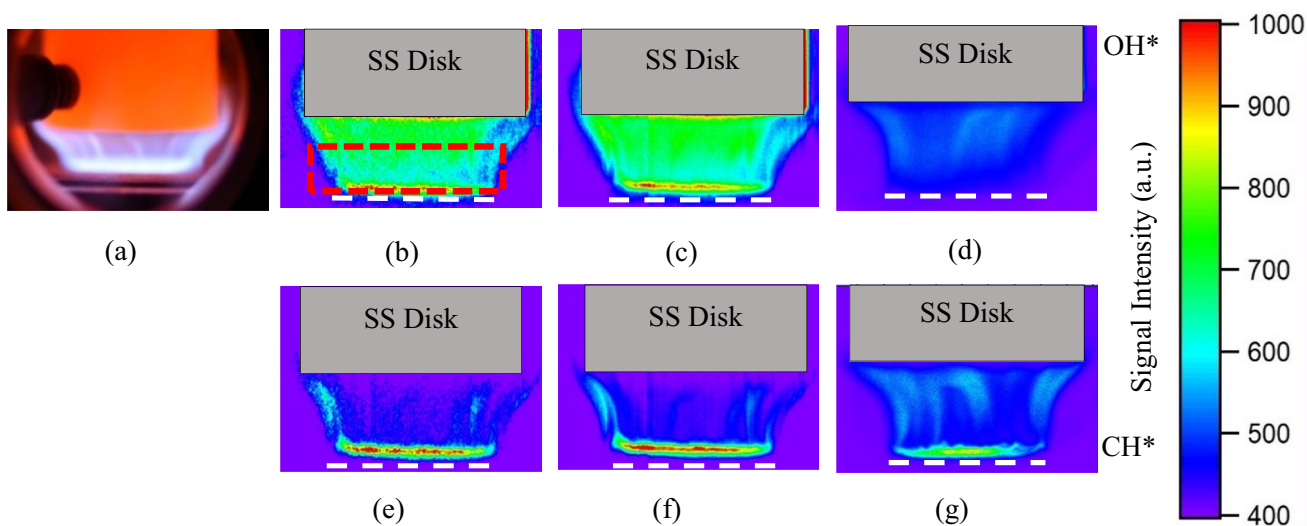


Fig. 6 Photo of experimental flame with a stabilizing stainless-steel disk **a**, false-color images of single shot image **b** and **e**, 1000 single-shot-averaged image **c** and **f**, and averaged image from an ICCD camera **d** and **g** at 8 bar $\phi = 1.2$ showing the elimination of flame oscillations

with the addition of a stabilizing disk. The red dashed line indicates the signal integration area (6.2 mm \times 19.2 mm). The white dashed lined represents the location of the burner surface

a. These images show the elimination of the flame oscillations allowing for better flame diagnostics and characterization. Additionally, the unstable flame in Fig. 5 shows asymmetrical features when the flame is at a minimum area, Fig. 5c. The addition of the stabilizing disk restored the symmetry of the flame as well as reduced flame oscillations.

Chemiluminescence images were analyzed by integrating the recorded signal in each frame. A $6.2 \text{ mm} \times 19.2 \text{ mm}$ integration zone, shown in Figs. 5 and 6, was used for both the stable and unstable chemiluminescence images. This integration zone was chosen to maximize the integration area while avoiding saturation from the stabilizing disk. Then, the integrated signal was normalized by the average signal across the integration zone from 1000 images. Figure 7 shows the normalized OH* chemiluminescence signal of the $\phi = 1.2$ flame at 8 bar plotted as a function of the frame number. The unstable flame OH* chemiluminescence signal demonstrated large low-frequency oscillations, while the stable flame demonstrated small high-frequency oscillations. The same trend is observed for CH* and broadband chemiluminescence. Using MATLAB's built-in fast Fourier transform (FFT) function, it was found that the dominant frequency of the unstable flame in Fig. 7 was 17 Hz, and the dominant frequency of the stable flame was 178 and 296 Hz. The same fast Fourier transform analysis was conducted for each pressure tested, revealing that as pressure was increased, the frequency of flame oscillations decreased from 19 Hz at 1 bar to 16 Hz at 10 bar. The high-frequency oscillations in the stable flame are likely due to either fluctuations in the flame due to the exhaust control valve and the PID loop controlling it or thermo-acoustic fluctuations inside the pressure vessel. Thermo-acoustic fluctuations similar to these have been studied using various techniques (Arndt et al. 2015; Meier et al. 2007).

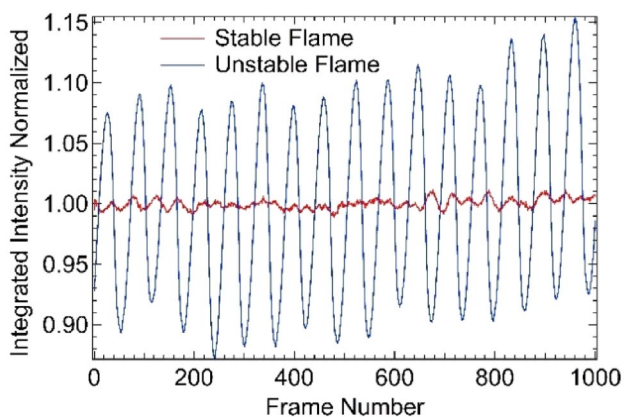


Fig. 7 Total normalized integrated OH* chemiluminescence signal of the stable and unstable $\phi = 1.2$ flame at 8 bar

Kostuick and Cheng discussed buoyancy-induced flame flickering. The interaction between the hot combustion products and relatively cold air co-flow drives buoyancy effects. Additionally, the air co-flow may have minor flow deformities leading to temperature differences in different portions of the burner, which could increase the buoyancy effects (Kostuick and Cheng 1994). Further investigation is needed to determine the cause of the high-frequency noise; however, the stabilizing disk reduced the large flame oscillations to allow for OH-LIF measurements. These flame oscillations are small enough in magnitude to not affect any experimental results.

3.2 OH-LIF imaging studies

A series of averaged OH fluorescence signals were detected in CH_4/air flames with operating pressures up to 10 bar. A study of the laser energy dependence shows a linear increase in the OH-LIF signal with the laser fluence until it reaches saturation in lower pressure conditions. To verify that the relationship between laser energy and the OH-LIF signal can be modeled linearly, the laser power was scanned in approximately $100\text{-}\mu\text{J}$ steps, and the fluorescence was collected for a $\phi = 1.2$ flame. The importance of achieving linearity lies in the fact that the fluence of the beam is not uniform throughout the projected sheet from the OH-LIF imaging setup. The laser fluence increases in the center and decreases steadily, moving toward the edge of the laser sheet. Therefore, if the total beam energy lies in the linear portion of the signal, the signal can be appropriately scaled across the beam sheet to account for decreased laser fluence near the edge of the beam sheet; this effectively creates a uniform top hat laser light sheet. In this study, the light sheet was first sent through an aperture to cut off the extreme edges of the beam where the laser energy significantly decreases. The remaining central region of the beam sheet was captured using a beam profiling camera (Spiricon, Model USB3-LT665), and this profile was used to correct for the nonuniformity in the beam sheet. Figure 8 shows that the relationship could be linear across the entire pressure range. The only discrepancy was in the 1 and 2 bar experiment, where the OH signal shows signs of partial saturation. Throughout the experiment, the laser energy was maintained at 0.8 mJ/pulse .

A wavelength scan was conducted to confirm the location of the $Q_1(7)$ rotational line in the (0,0) band and to compare with excitation profiles generated from LIFBASE (Luque and Crosley 1999). The $Q_1(7)$ rotational line was selected based on previous work by Boxx et al. (2015). Line broadening due to elevated pressure inside the burner is present and observable in Fig. 9. The absorption line shape of the OH radical is most commonly described by a Voigt profile at higher pressures due to both Doppler and collisional broadening mechanisms. As the pressure increases, the collisional

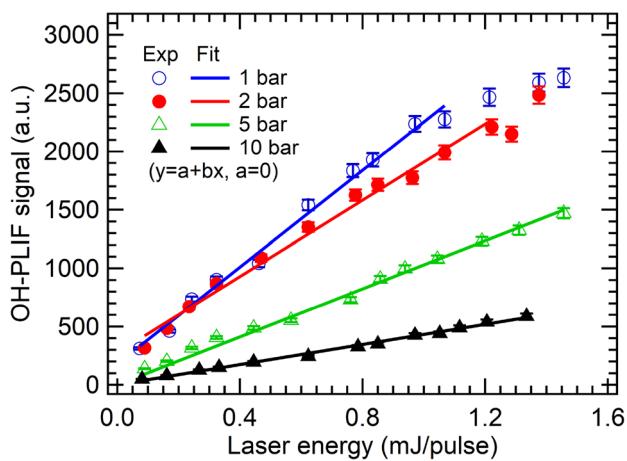


Fig. 8 OH-LIF laser pulse energy dependence

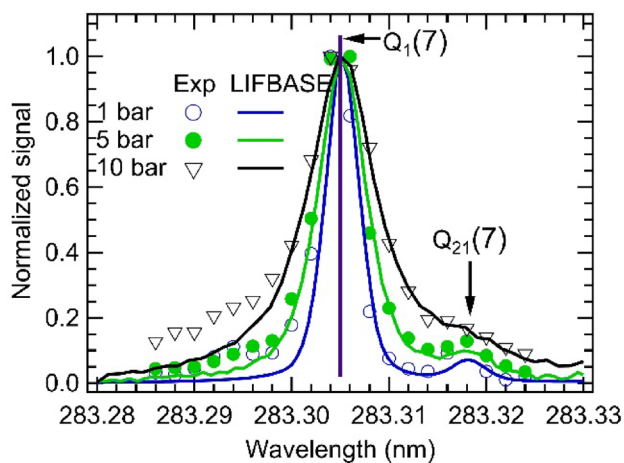


Fig. 9 OH-LIF excitation wavelength scan

broadening will take over, and the spectrum should become broader (Davidson et al. 1996; Tu et al. 2020). The line broadening at increased pressure seen in this work was similar to other experimental results in the literature, but red shifting was not observed (Kohse-Höinghaus et al. 1990; Davidson et al. 1996; Tu et al. 2020).

As mentioned previously, OH-LIF images were recorded with an ICCD camera equipped with a 315 ± 7.5 nm filter to detect the 308 nm fluorescence signal from the $A \leftarrow X$ (1,1) and (0,0) bands. Figure 10 shows the flames at 2, 5, and 10 bar with varying equivalence ratios. The flame is premixed, and the leaner equivalence ratios accurately represent ideal premixed behavior with a consistent combustion zone across the whole surface of the burner to the bottom of the stabilization disk. However, starting at 2 bar $\phi = 1.05$, 5 bar $\phi = 0.95$, and 10 bar $\phi = 0.95$ cases, the middle section of the signal started to deteriorate, indicating that the

reaction zone was shifting toward the edges of the burner rim where the air co-flow is exiting. This behavior was consistent with other diffusion flames found in the literature (Zhao et al. 2018). The co-flow closest to the flame in our configuration consisted of air which provided the possibility of another reaction zone becoming evident in the wings of the premixed flame. Another item to note is that the signal decreased significantly with increasing pressure, as shown by the scale factor of each image below applied during data processing. This trend has been documented in other studies and is to be expected due to the already mentioned collisional quenching effects increasing with pressure along with signal trapping increasing with pressure, thus reducing the signal (Kohse-Höinghaus et al. 1990; Davidson et al. 1996; Tu et al. 2020). Yin and co-workers (Yin et al. 2014) suggested that signal trapping can be minimized through (1,0) excitation and (1,1) detection, which is the general excitation and detection scheme used in this work. However, the bandpass filter used in this work also captures some emissions from the (0,0) band after vibrational energy transfer, which may increase the effect of signal trapping. At elevated pressure, the assumption of minimal signal trapping cannot be applied, and the effect of signal trapping should be evaluated using Eq. 6 in Yin et al. Future works will focus on the effects of signal trapping to better quantify the OH-LIF signal.

Experimental data were taken at the $Q_1(5)$ and $Q_1(14)$ rotational lines of the $OH A^2\Sigma^+ \rightarrow X^2\Pi(1,0)$ electronic transitions for use in thermometry measurements which will be discussed later in this work. Previous results have indicated that this pair of lines yield the most accurate OH-LIF thermometry results (Wang et al. 2019b). Radial data was taken from the $Q_1(5)$ scan and presented below in Fig. 11. The scans confirmed the conclusions drawn from Fig. 10. At the fuel-rich case of $\phi = 1.2$, the OH-LIF signal in the center decreases significantly to almost zero. This phenomenon is because the premixed flow into the burner is rich, and combustion decreases in the center. The excess fuel makes its way to the edges of the burner surface, where the co-flow of air is propagating. This creates a pocket of combustion on the outside of the premixed flame. This pocket of combustion is why the $\phi = 1.2$ flame, near the radial distance of ± 10 mm, there are two prevalent peaks. This behavior is usually noted in diffusion flames, which will require more investigation in the future. The presence of the stabilization disk undoubtedly played a significant role in changing the flame structure at higher equivalence ratios and helped with trapping the combustion in the pockets observed. The $\phi = 1.2$, 2 bar flame is noticeably asymmetric, and the same flame at 5 and 10 bar is also slightly asymmetrical. The asymmetry can be explained by flame distortion issues with the burner itself not exhibiting fully symmetric properties, which are more easily seen at lower pressure, causing the

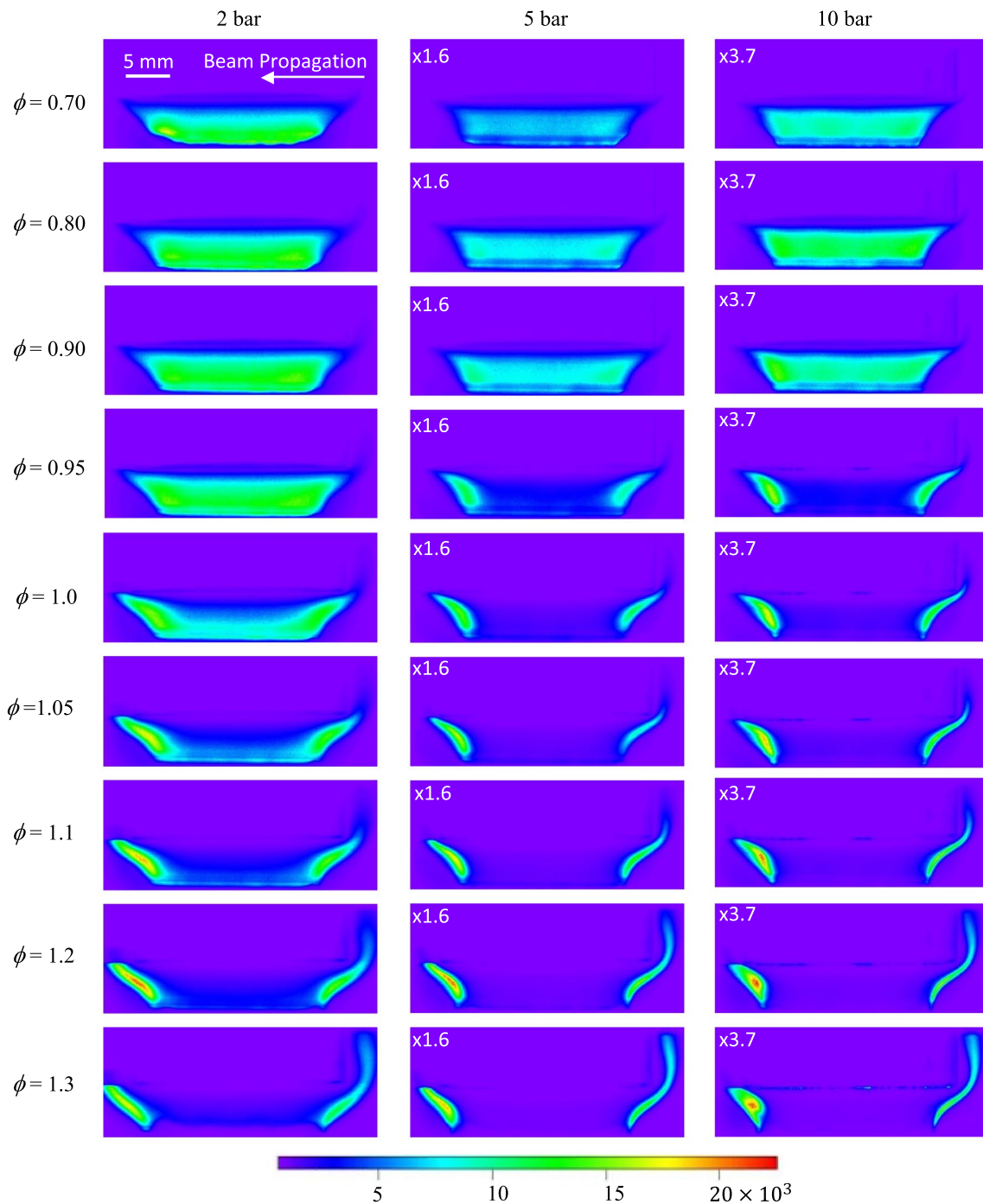


Fig. 10 Time averaged OH-LIF images at 2, 5, and 10 bar

discrepancy. These conditions may stem from slight misalignments of the disk or nonuniformities in the porous burner surface, which are addressed in the ongoing modifications to the burner assembly.

4 Discussion

4.1 OH-LIF pressure scaling: 1–10 bar

One of the significant effects responsible for the disparity in the images in Fig. 10 during OH-LIF measurements at higher pressures is the collisional quenching (Q) effect. Quenching rates have been experimentally determined.

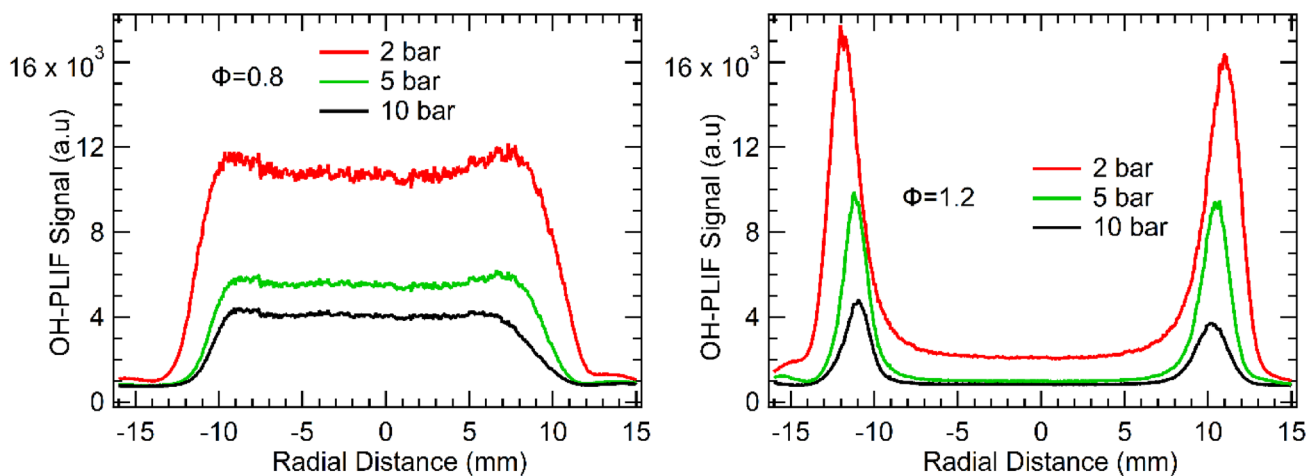


Fig. 11 Radial plots of OH signal at the Q1(5) wavelength for $\phi=0.8$ (left) $\phi=1.2$ (right) flames at 2, 5, and 10 bar

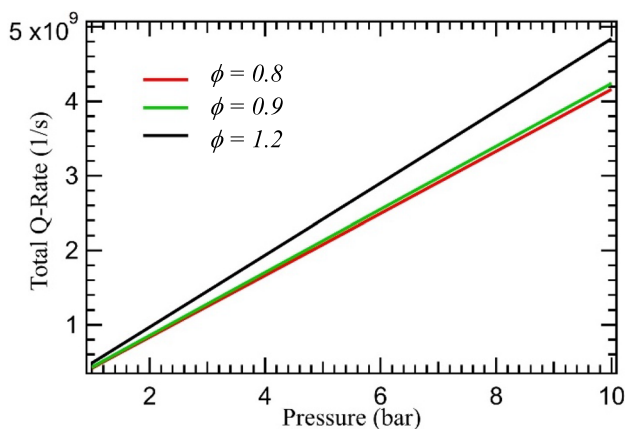


Fig. 12 Graphical representation of quenching rates in premixed flame environments

These rates are then used to calculate quenching rates at elevated pressures. In this work, we calculated the quenching rates at different pressures considering CH_4 , H_2O , CO_2 , O_2 , H_2 , and CO to be the major colliders. The concentrations of these species and temperatures were simulated using the CANTERA equilibrium code. Species concentrations and temperatures from the simulation do not definitely represent the profiles of premixed CH_4 /air flames stabilized on the burner with cooling water flowing in/out of the burner disk and are also affected by the suitability of the flame kinetic mechanism used for modeling the combustion process (Goodwin et al. 2021). The corresponding temperature- and pressure-dependent cross sections were determined based on a “harpooned model” proposed by Paul (1994). In this model, the coefficient for quenching of OH by N_2 is zero, thus not contributing to the collisional quenching of OH-LIF signals. The assumption of negligible or zero quenching from N_2 is consistent with other OH-LIF studies

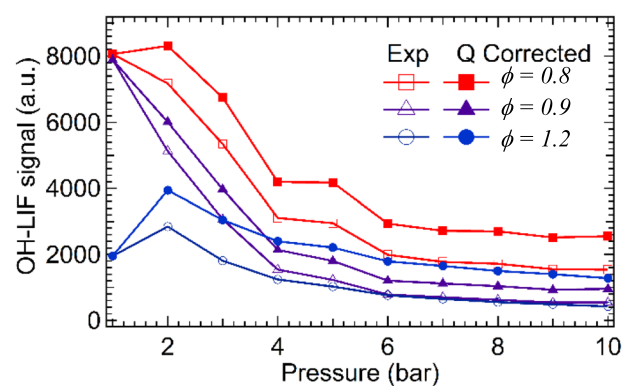


Fig. 13 Quenching-corrected OH-LIF signals as a function of pressure

at elevated pressure (Escofet-Martin et al. 2022). The calculated quenching rates are shown in Fig. 12; it can be seen that the quenching rate varies with equivalence ratio and pressure. The resulting quenching rates agree well with previously reported values (Tu et al. 2020).

After applying quenching corrections for OH signals at different pressures, the total integrated OH signals are shown in Fig. 13. It is seen that the variations of quenching-corrected OH-LIF signals follow the same trends seen in the uncorrected data for all pressure conditions. Other negative effects, such as line broadening and signal trapping, must be considered to fully explain the reduced OH-LIF signal. In addition, the UV absorption has little influence based on the symmetry of radial profiles of OH-LIF images, as seen in previous publications (Tu et al. 2020). The OH-LIF signal symmetry in the radial profiles can be seen in Fig. 11, especially in lean low-pressure flames. In higher-pressure and richer flames, the profiles became less symmetric because of irregularities in the flame itself. The flame irregularities

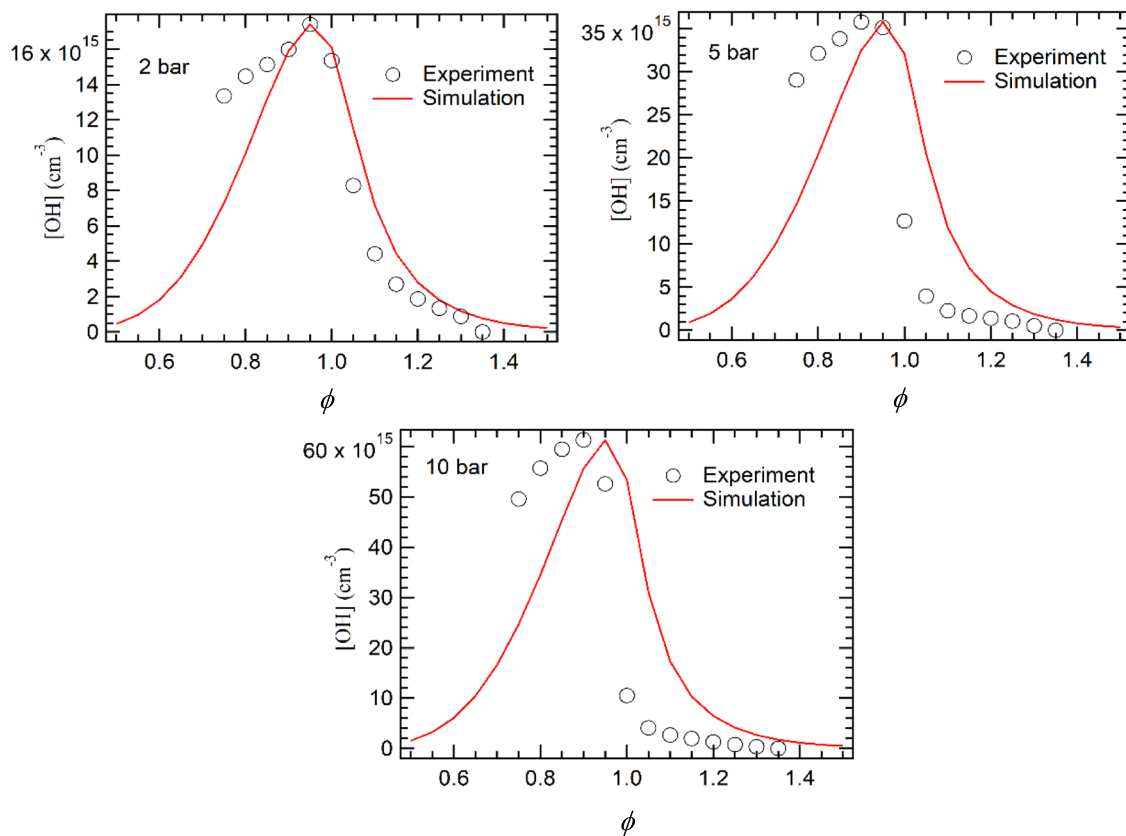


Fig. 14 Quenching corrected OH-LIF signal as a function of the equivalence ratio at pressures of 2, 5, and 10 bar

can be seen in Fig. 10, where the OH-LIF signal is stronger on the far side of the flame with respect to the laser beam. If laser absorption was a major factor, the signal on the far side of the flame would be weaker.

One point of interest was the correlation of the strength of the OH-LIF signal to the equivalence ratio. Combustion efficiency is maximized at $\phi = 1.0$, and therefore, the highest OH-LIF signal should occur here as well. Figure 14 shows the number density of the OH radical at three different pressures while varying the equivalence ratio. This data suggests that the peak OH-LIF signal occurs during lean combustion. The experimental data are plotted against CANTERA simulations (Goodwin et al. 2021). Measurements were obtained by integrating the premixed region of the OH-LIF images to avoid any OH produced in the diffusion flame region. Since the uncorrected experimental data was taken from the premixed region, OH quenching calculations presented earlier can be applied. Quenching-corrected measurements are compared qualitatively with the maximum OH number density from the corresponding Cantera simulation. The experimental and model results were similar in the trend line shape presented, yet the experimental data peak appeared to be shifted leaner than predicted in the model. After the experiment was completed, calibration was done on the

MKS mass flow controllers to get an accurate reading of the actual flow rates coming in to see if it could account for the issue. The flowmeters were calibrated by flowing the gas into an inverted container filled with water supported in a water bath and measuring the time for a given volume displacement. The calibration test suggested that the equivalence ratio should be shifted by $\phi = 0.05$ to the richer side for each case to offset the inconsistency in the mass flow controller. That offset is reflected in Fig. 14, and for the cases of 5 and 10 bar, the offset is still insufficient to match the results. The increasing pressure in the system undoubtedly contributed to the increased uncertainty and shift in ratio.

4.2 OH-LIF thermometry

Temperature measurements were taken to further characterize the flame. Other research has already investigated higher-pressure flame thermometry and showed promising results at leaner equivalence ratios (Attal-Trétout et al. 1990; Kohse-Höinghaus et al. 1990; Wang et al. 2019b) also using NO as target species (Bessler et al. 2002a, b). Attal-Trétout et al. (1990) and Kohse-Höinghaus et al. (1990) took CARS and LIF-thermometry in a twin burner, although using other flow rates and without inserting a stabilization disk.

As mentioned before, for the two-color thermometry procedure, the $Q_1(5)$ (at 282.750 nm) and $Q_1(14)$ (at 286.456 nm) rotational transitions of the OH $A^2\Sigma^+ - X^2\Pi$ (1,0) band were used, followed by detecting the fluorescence emission in the OH $A^2\Sigma^+ - X^2\Pi$ (0,0) and (1,1) bands. The ratio of average OH-LIF signals from the transition lines was used to determine the theoretical temperature based on the technique discussed by Wang and co-workers (Wang et al. 2019b). The temperature dependence of the $Q_1(5)$ to $Q_1(14)$ ratio was calibrated using LIFBASE at 1 bar using a power law fit (Wang et al. 2019b). Figure 15 shows the temperature distribution of the flame at 2 and 10 bar. Since the ability to measure the temperature depends on the OH concentration, in areas of low OH concentration, the signal-to-noise ratio of the two-line thermometry approach is too low to predict the temperature confidently. In Fig. 15, these areas are labeled undefined. This is also the reason why some areas show a temperature of 3000 K, which is unrealistic for a methane flame. According to Wang et al., this technique, with an appropriate OH-LIF signal, could accurately measure temperatures between 800 and 3000 K (Wang et al. 2019b). The temperatures of the 10-bar flame were significantly higher than the 2-bar flame, but the 2-bar flame had a more homogeneous structure. At the richer flame equivalence ratios for 10 bar, the temperature is undefined in the center, consistent with the results presented earlier. This also provides further evidence of the absence of the flame front and decrease in combustion in the central area at these equivalence ratios.

The temperature fields in Fig. 15 provide information on the temperature distribution as a function of the radial distance and HAB. Figure 16 shows the resulting radial and axial temperature profiles of the flame at different ϕ and pressures with colored solid lines. It further demonstrates that the radial position temperatures depended heavily on ϕ and pressure. These figures indicated the temperature increased at higher pressures, which is true in some cases studying the NO concentration in high-pressure flames (Bessler et al. 2002a, b). The stabilizing disk most likely had a large part in the temperature increase at higher pressure because the disk tends to trap heat and radiate back to the burner surface. One item of note is the fact that the temperature appeared constant throughout the center for all pressures. However, this observation is not altogether surprising as the previously presented images indicate a uniform temperature distribution at the leaner equivalence ratios. Axial temperature distributions seemed to be consistent for pressure variation with a fixed equivalence ratio which also agreed with previously produced images. The axial temperature profiles in Fig. 16c and d show that for lean flames, the temperature profile follows a similar trend for the three pressures tested. The temperature starts high near the burner surface, then quickly drops before increasing again higher up in the flame. The temperature then decreases when approaching the stabilizing disk. This general trend is not observed in rich flames in Fig. 16d, which can be attributed to the uncertainty of the OH thermometry technique. In

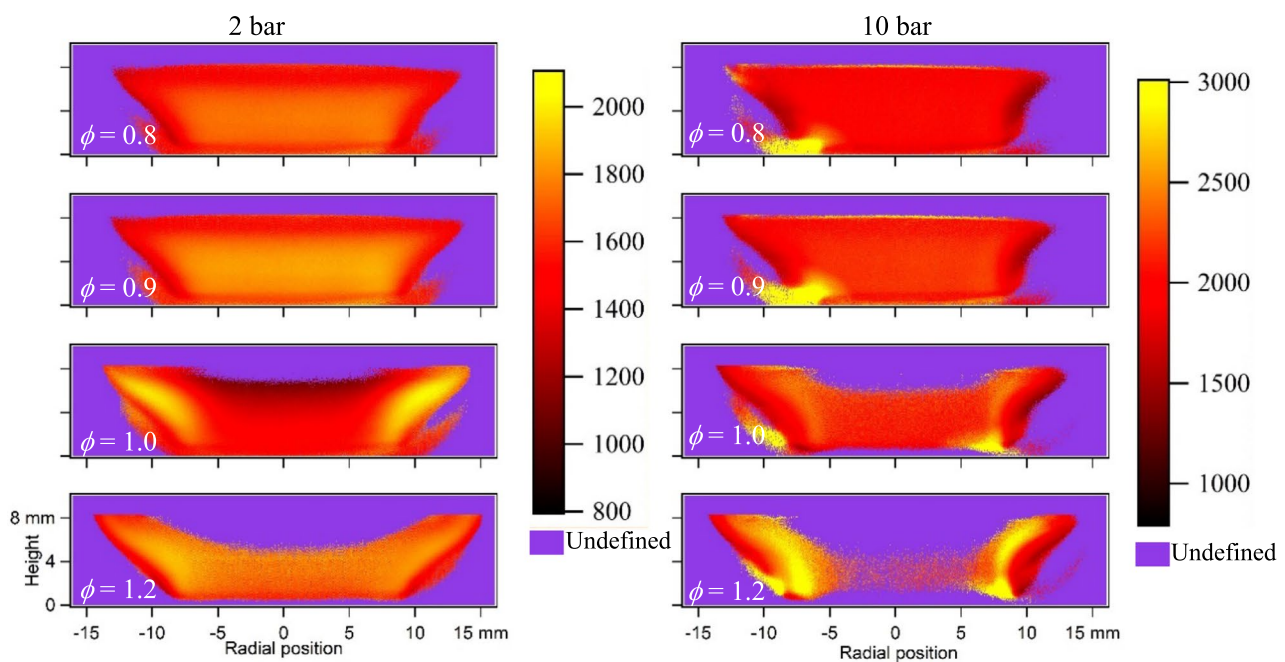


Fig. 15 Temperature plots (K) using two-color OH-LIF thermometry at 2 bar (left) and 10 bar (right). Low concentrations of OH resulted in low signal to noise ratios and undefined temperature measurements

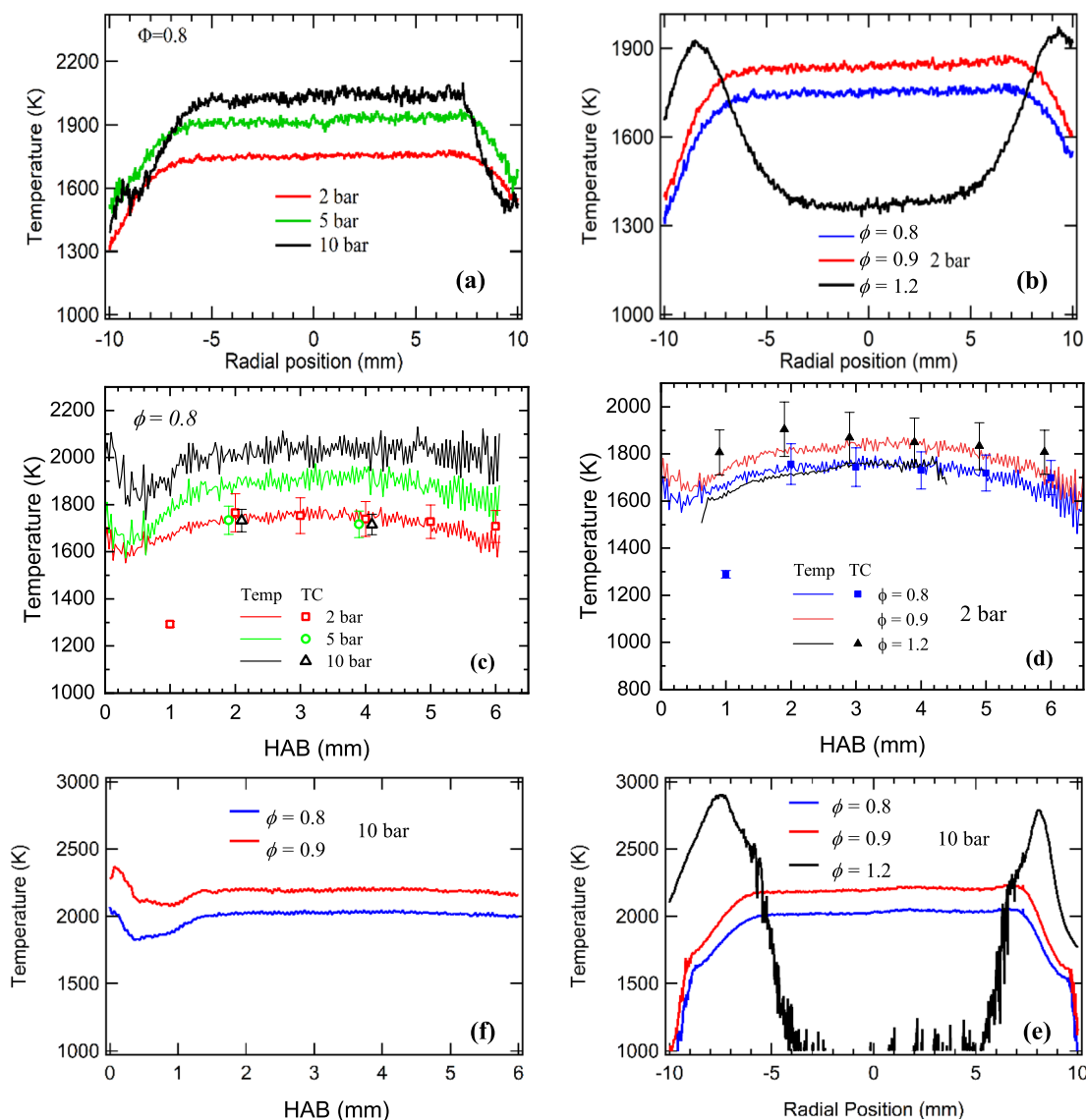


Fig. 16 Radial temperature plots recorded 4 mm above the burner surface in **a** $\phi=0.8$ flames for different pressures and **b** 2-bar flames for different ϕ . Temperature trends recorded with OH-LIF (solid

lines) and TC measurements (symbols) at different HAB locations are shown in panels **c** & **d**. Similarly radial and axial temperature profiles are plotted for different ϕ **e** & **f**

rich flames, the OH-LIF signal decreased substantially in the center of the flame as the combustion reaction moved toward the wings of the flame. Temperature profiles at 10 bar are shown in Fig. 16e and f. The radial profiles in Fig. 16e highlight the observation of constant temperature in the center of the flame for lean flames and an undefined temperature region in the center of rich flames. Axial profiles at 10 bar were limited to lean flames because of the before mentioned undefined temperature region. This decrease in the OH-LIF signal makes the temperature evaluation in the middle portion of the rich flames unrealistic.

4.3 Thermocouple measurements

For some of the flame conditions listed in Table 1 and corresponding to the temperature profiles in Fig. 16c and d, radiation-corrected thermocouple (TC) measurements of gas-phase temperature were carried out with coarse steps in the HAB position and compared with the respective OH-LIF results. The plotted values (symbols) are the mean resulting from the gas temperatures calculated using Eq. (1), and Eq. (2) with the Nu-correlations expressed in Eqs. (3) and (4), respectively, in Sect. 2.2. Error bars represent the calculated standard deviations from this averaging, but do not include systematic errors and uncertainties

inherent in several of the parameters included in Eqs. (1)–(4). Figure 16c shows the temperature variation as a function of HAB and for pressures of 2, 5, and 10 bar at $\phi = 0.8$. At $HAB \geq 2$ mm, both OH-LIF thermometry and thermocouple measurements show an almost constant temperature; however, the TC measurements do not show the increasing temperature plateau with pressure seen in the OH-LIF temperatures, while the TC-derived temperature at 1 mm HAB is significantly lower. The higher temperatures close to the burner surface (closer to the flame front below 1 mm HAB) cannot be accessed by the bulky TC bead. It is also observed that the TC-derived temperatures do not vary much with total pressure, with a possible reason being the neglect of heat loss by conduction through the wires (Shaddix 2017). With respect to ϕ and at a constant pressure of 2 bar (Figs. 15 and 16d) the TC data for $\phi = 0.8$ are in quite good agreement with the profile from OH LIF, however, the $\phi = 1.2$ data are higher than the ones derived from OH LIF, which are indistinguishable within the measurement range from the $\phi = 0.8$ profile. Also, the trend of a temperature increase with ϕ and a subsequent decrease is visible in the OH-LIF measurements but at a larger ϕ than typically expected from thermophysical calculations. Radial TC-derived temperature profiles (not shown) also do not show this significant dip in the center

region seen in Fig. 16b at $\phi = 1.2$, but only a small dip (less than 100 K) at a larger $\phi = 1.6$. These differences in results between the two techniques could be due to the non-exact operating conditions of the two burners at Texas A&M and Duisburg-Essen Universities, the modest spatial resolution of the TC (bead diameter 200 μm), and the missing conduction heat-loss correction.

4.4 Comparison with ANSYS fluent simulation

The experimental OH-LIF results were compared to the OH distribution simulated with ANSYS Fluent. Figure 17 shows the qualitative comparison of the OH signal and mole fraction obtained from the experiment and the model, respectively. The model prediction shows that OH concentration distribution is centered during lean combustion. During rich combustion, the simulated distribution replicates the high peripheral OH concentration seen in the experiments, thus strengthening the credibility of the results obtained from the experimental data. There is a slight discrepancy in the stoichiometric case at 10 bar. The experimental results show OH concentrated on the edge of the flame with very little in the center of the flame. In contrast, the simulation shows an even distribution throughout the flame.

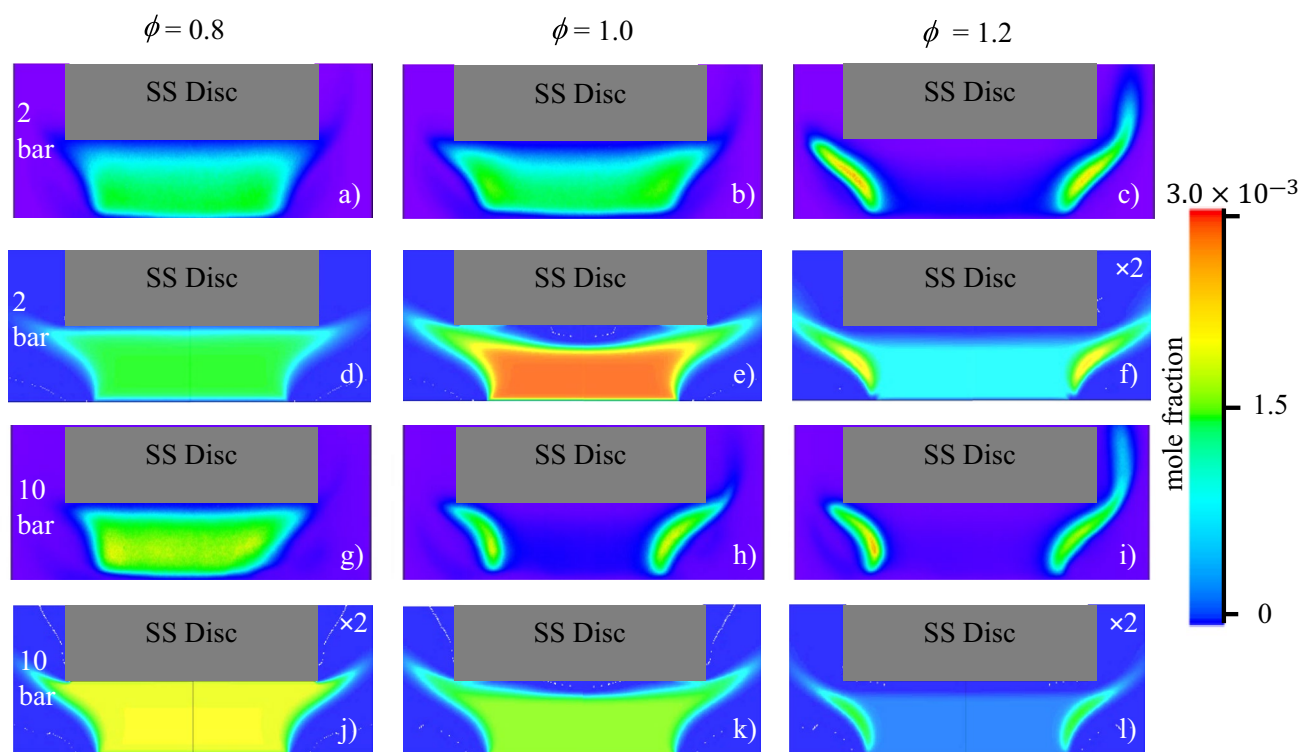


Fig. 17 Qualitative comparison of OH concentrations for CH_4/air flame at 2 bar **a–f** and 10 bar **g–l** recorded for $\phi = 0.8$ (left), $\phi = 1.0$ (middle), and $\phi = 1.2$ (right). Images **a–c** and **g–i** represent OH sig-

nal obtained from the experiment and images **d–f** and **j–l** represent simulated OH mole fraction distributions for 2 and 10 bar respectively

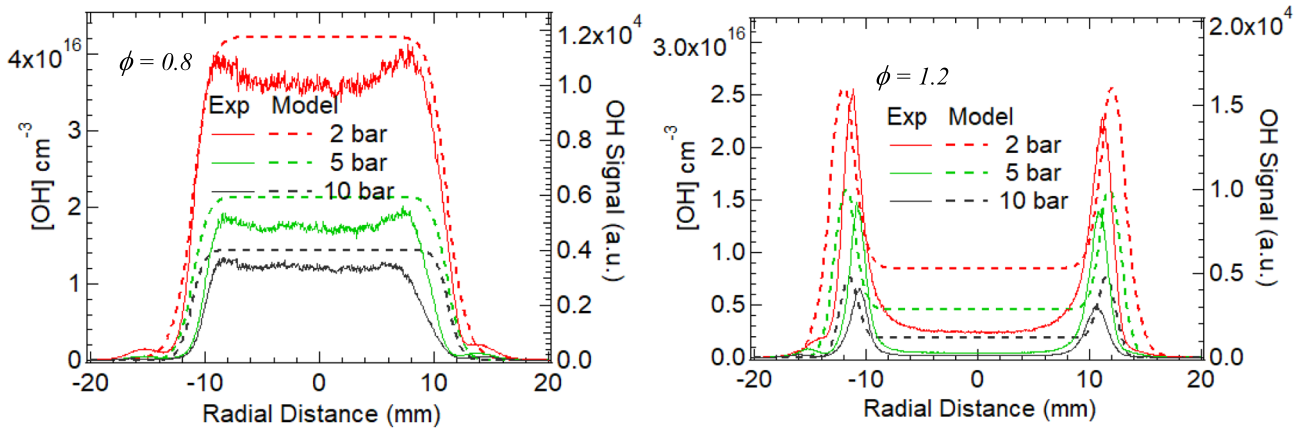


Fig. 18 Quantitative comparison of radial OH concentration profiles measured for different pressures at HAB=4 mm for $\phi=0.8$ (left) and $\phi=1.2$ (right). The model data at 2 bar are scaled up by factors

4 and 3 for lean and rich case respectively. Similarly, the model data at 10 bar are scaled down by factors 2.5 and 3.5 for the lean and rich case, respectively, while keeping the model data at 5 bar constant

Radial profiles allow for a better quantitative comparison between the experimental and simulated results. Figure 18 is a visual representation of the radial distribution of OH-LIF for $\phi=0.8$ and 1.2. As seen previously in the images in Fig. 10, the signal from the lean equivalence ratios is more evenly distributed throughout the flame compared to profiles from rich flames. The shape of the models agreed with the experimental data, but the models had to be scaled to match the trends correctly. The signal appears to almost decrease to zero at higher pressures in both the model and experimental profiles, which is also consistent with the background-subtracted images from Fig. 10.

Quantitative comparisons of the experimental and modeled temperature are displayed in Fig. 19. The matching shape of the model and experimental data was promising, as the majority of the lines appeared to reflect the experimental results acquired when a scaling factor was applied. For the experimental axial temperature profiles, the temperature first increased by around 100–200 K in the center of the flame and slowly decreased again. This trend held for most equivalence ratios except at $\phi=1.0$, where the temperature consistently decreased. The radial temperature plot in Fig. 19 is similar to Fig. 16b above, in which the modeled lean flames showed a consistent temperature profile. However, for the rich flames ($\phi=1.2$), the experimental temperature is undetermined in the middle portion due to the lack of OH.

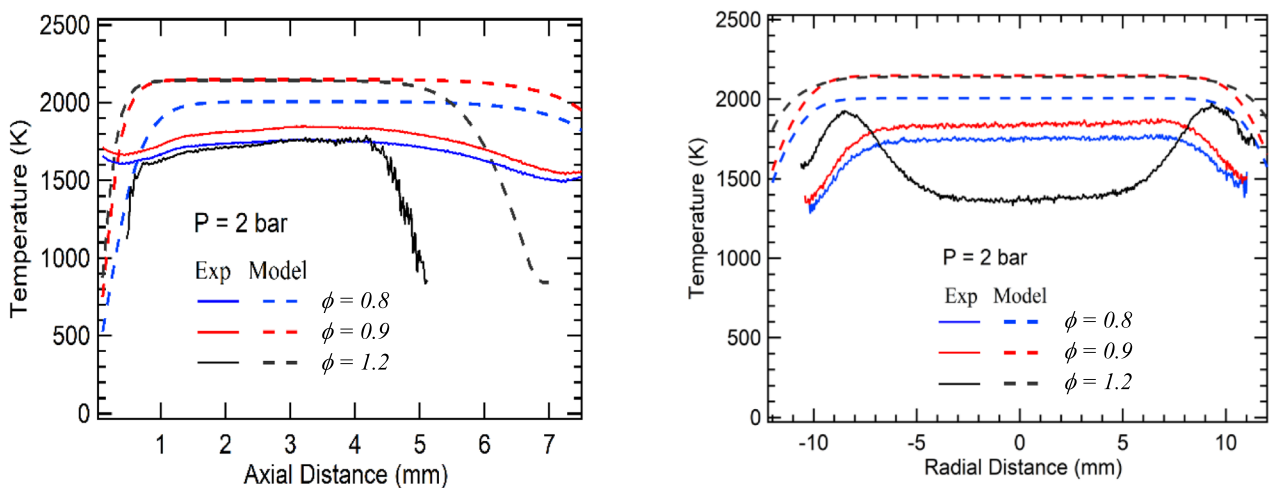


Fig. 19 Quantitative comparison of temperature profiles recorded along the flame axis (left) and along the flame radius at HAB=4 mm (right)

5 Conclusions

This work reports the characterization of a high-pressure burner facility using chemiluminescence, OH-LIF imaging, and two-color OH-LIF thermometry. For chemiluminescence images, three different emission bands, total chemiluminescence, OH* and CH* were recorded using suitable bandpass filters. These chemiluminescence measurements revealed the flame oscillations of premixed CH₄/air flames and subsequent flame stabilization by adding a stainless-steel disk above the flat flame. Subsequently, OH-LIF imaging was used to record the reaction zone of the high-pressure flames between 1 and 10 bar. The hydroxyl radical was excited via the Q₁(7) rotational transition of the OH A²Σ⁺←X²Π (1,0) electronic band, and for the thermometry measurements, the LIF intensity ratio after excitation of the Q₁(5) and Q₁(14) rotational transitions was used. Thermocouple temperature measurements were also performed at selected locations and compared with two-color OH thermometry results. The OH-LIF experiments demonstrated several key features of the flame that were consistent with the literature. Pressure-broadened line shapes followed the model predictions generated using the LIFBASE simulation package. With the increase in the equivalence ratio ϕ , the transition from fully premixed to partially premixed and diffusion flame behavior was observed. This behavior was evident during the initial imaging phase, where the OH signal at higher ϕ and higher pressures reduced to almost zero in the middle of the burner and started to resemble more of a diffusion-like flame. OH-LIF can be used in the future to optimize the stabilizing disk position for improved flame stability. A detailed quenching correction was required to account for the signal loss from collisional quenching mechanisms that decreased the intensity of the signal significantly as pressure increased. Measurements show the OH-LIF signal peaked near $\phi = 0.95$ at 10 bar, but the combustion chemistry dictates the OH number density is significantly higher compared to lower pressures. The higher number density should result in a higher OH-LIF signal, however, laser-beam absorption and fluorescence signal trapping reduce the fluorescence yield. Two-color OH-LIF thermometry measurements revealed the high-temperature zone moving away from the center at higher ϕ , consistent with the prediction of computational flame simulations. At lean flames, the temperature distributions were nearly uniform across the radial distance of the flame. The present study establishes an optically accessible high-pressure burner facility to investigate the effect of the minor species on soot nucleation chemical pathways in realistic gas-turbine or internal combustion-engine-related flame conditions.

Authors' contributions All authors contributed to the conception and design of the study. Material preparation, data collection, and analysis were performed by Will Swain, Yejun Wang, Pradeep Parajuli, Matthew Hay, and Ahmad Saylam. The first draft of the manuscript was written by Will Swain, and all authors commented on previous versions of the manuscript. All authors read and approved the final manuscript.

Funding The authors acknowledge the funding support provided by the U. S. National Science Foundation (grant# CBET-1604633) and the German Research Foundation (project number 439059510: "Soot nucleation in low-sooting high-pressure flames: Experiment and modeling").

Data availability Original datasets can be obtained for any valid reason by directly contacting the corresponding author.

Declarations

Conflict of interest All the authors declare that there is no conflict of interest.

References

- Anslys Chemkin-Pro (2023), Chemistry Simulation Software. From <https://www.ansys.com/de-de/products/fluids/ansys-chemkin-pro>
- Arndt CM, Severin M, Dem C, Stohr M, Steinberg AM, Meier W (2015) Experimental analysis of thermo-acoustic instabilities in a generic gas turbine combustor by phase-correlated PIV, chemiluminescence and laser Raman scattering measurement. *Exp Fluids* 56:69. <https://doi.org/10.1007/s00348-015-1929-3>
- Atakan B, Heinze J, Meier UE (1997) OH Laser-induced fluorescence at high pressures: spectroscopic and two-dimensional measurements exciting the A-X (1,0) transition. *Appl Phys B* 64:585–591. <https://doi.org/10.1007/s003400050219>
- Attal-Trétout B, Schmidt SC, Crete E, Dumas P, Taran JP (1990) Resonance CARS of OH in high-pressure flames. *J Quant Spec Rad Transfer* 43:351–364. [https://doi.org/10.1016/0022-4073\(90\)90001-M](https://doi.org/10.1016/0022-4073(90)90001-M)
- Bessler WG, Schulz C, Lee T, Jefferies JB, Hanson RK (2002a) Strategies for laser-induced fluorescence detection of nitric oxide in high-pressure flames. I. A-X(0,0) excitation. *Appl Opt* 40:3547–3557. <https://doi.org/10.1364/AO.41.003547>
- Bessler WG, Schulz C, Lee T, Shin DI, Hofmann M, Jeffries JB, Wolfrum J, Hanson RK (2002b) Quantitative NO-LIF imaging in high-pressure flames. *Appl Phys B* 75:97–102. <https://doi.org/10.1007/s00340-002-0946-0>
- Betrancourt C, Aubagnac-Karkar D, Mercier X, El-Bakali A, Desgroux P (2022) Experimental and numerical investigation of the transition from non sooting to sooting premixed n-butane flames, encompassing the nucleation flame conditions. *Combust Flame* 243:112172. <https://doi.org/10.1016/j.combustflame.2022.112172>
- Boxx I, Slabaugh C, Kutne P, Lucht RP, Meier W (2015) 3 kHz PIV/OH-PLIF measurements in a gas turbine combustor at elevated pressure. *Proc Combust Inst* 35:3793–3802. <https://doi.org/10.1016/j.proci.2014.06.090>
- Cai W, Li X, Ma L (2013) Practical aspects of implementing three-dimensional tomography inversion for volumetric flame imaging. *Appl Opt* 52:8106–8116. <https://doi.org/10.1364/AO.52.008106>
- Carter CD, Laurendeau NM (1994) Wide- and narrow-band saturated fluorescence measurements of hydroxyl concentration in premixed flames from 1 bar to 10 bar. *Appl Phys B* 58:519–528. <https://doi.org/10.1007/BF01081084>

- Collis DC, Williams MJ (1959) Two-dimensional convection from heated wires at low Reynolds numbers. *J Fluid Mech* 6:357–384
- Davidson DF, Roehrig M, Petersen EL, Di Rosa MD, Hanson RK (1996) Measurements of the OH A-X (0,0) 306 nm absorption bandhead at 60 atm and 1735 K. *J Quant Spect Radiat Transfer* 55:755–762. [https://doi.org/10.1016/0022-4073\(96\)00024-6](https://doi.org/10.1016/0022-4073(96)00024-6)
- Devillers R, Bruneaux G, Schulz C (2008) Development of a two-line OH-laser-induced fluorescence thermometry diagnostics strategy for gas phase temperature measurements in engines. *Appl Opt* 47:5871–5885. <https://doi.org/10.1364/AO.47.005871>
- Do H-Q, Tran L, Gasnot L, Mercier X, El-Bakali A (2021) Experimental study of the influence of hydrogen as a fuel additive on the formation of soot precursors and particles in atmospheric laminar premixed flames of methane. *Fuel* 287:119517. <https://doi.org/10.1016/j.fuel.2020.119517>
- Dulin V, Sharaborin D, Tolstoguzov R, Lobasov A, Chikishev L, Markovich D, Wang S, Fu C, Liu X, Li Y, Gao Y (2021) Assessment of single-shot temperature measurements by thermally-assisted OH PLIF using excitation in the $A^2\Sigma^+-X^2\Pi(1,0)$ band. *Proc Combust Inst* 38:1877–1883. <https://doi.org/10.1016/j.proci.2020.07.025>
- Escofet-Martin D, Chein Y, Dunn-Rankin D (2022) PLIF and chemiluminescence in a small laminar coflow methane-air diffusion flame at elevated pressures. *Combust Flame* 243:112067. <https://doi.org/10.1016/j.combustflame.2022.112067>
- Frank JH, Miller MF, Allen MG (1999) Imaging of laser-induced fluorescence in a high-pressure combustor. *AIAA Aero Sci.* <https://doi.org/10.2514/6.1999-773>
- Gaseq (2023), A chemical equilibrium program for windows. From <http://www.gaseq.co.uk/>
- Goodwin DG, Speth RL, Moffat HK, Weber BW (2021) Cantera: An object-oriented software toolkit for chemical kinetics, thermodynamics, and transport processes. Version 2.5.1. <https://www.cantera.org>
- GRI-Mech (2023). from <https://chemistry.cerfacs.fr/en/chemical-database/mechanisms-list/gri-mech-3-0/>.
- Hindasageri V, Vedula RP, Prabhu SV (2013) Thermocouple error correction for measuring the flame temperature with determination of emissivity and heat transfer coefficient. *Rev Sci Instr* 84:024902. <https://doi.org/10.1063/1.4790471>
- Hofmann M, Bessler WG, Schulz C, Jander H (2003) Laser-induced incandescence for soot diagnostics at high pressures. *Appl Opt* 42:2052–2062. <https://doi.org/10.1364/AO.42.002052>
- Jain A, Wang Y, Schweizer C, Kulatilaka WD (2021) Simultaneous imaging of H and OH in flames using a single broadband femtosecond laser source. *Proc Combust Inst* 38(1):1813–1821. <https://doi.org/10.1016/j.proci.2020.07.137>
- Kaskan WE (1957) The dependence of flame temperature on mass burning velocity. *Symp (intl) Combust* 6:134–143. [https://doi.org/10.1016/S0082-0784\(57\)80021-6](https://doi.org/10.1016/S0082-0784(57)80021-6)
- Kim TY, Kim YH, Ahn YJ, Choi S, Kwon OC (2019) Combustion stability of inverse oxygen/hydrogen coaxial jet flames at high pressure. *Energy* 180:121–132. <https://doi.org/10.1016/j.energy.2019.05.089>
- Kohse-Höinghaus K, Meier U, Attal-Trétout B (1990) Laser-induced fluorescence study of OH in flat flames of 1–10 bar compared with resonance CARS experiments. *Appl Opt* 29:1560–1569. <https://doi.org/10.1364/AO.29.001560>
- Kojima J, Ikeda Y, Nakajima T (2005) Basic aspects of OH(A), CH(A), and C₂(d) chemiluminescence in the reaction zone of laminar methane-air premixed flames. *Combust Flame* 140:34–45. <https://doi.org/10.1016/j.combustflame.2004.10.002>
- Kostiuk LW, Cheng RK (1994) Imaging of premixed flames in microgravity. *Exp Fluids* 18:59–68. <https://doi.org/10.1007/BF00209361>
- Kramers H (1946) Heat transfer from spheres to flowing media. *Physica* 12:61–80
- Krishnan S, Kumfer BM, Wu W, Li J, Nehorai A, Axelbaum RL (2015) An approach to thermocouple measurements that reduces uncertainties in high-temperature environments. *Energy Fuels* 29:3446–3455. <https://doi.org/10.1021/acs.energyfuels.5b00071>
- Kuehner JP, Naik SV, Kulatilaka WD, Chai N, Laurendeau NM, Lucht RP, Scully MO, Roy S, Patnaik AK, Gord JR (2008) Perturbative theory and modeling of electronic-resonance-enhanced coherent anti-Stokes Raman scattering spectroscopy of nitric oxide. *J Chem Phys* 128:174308. <https://doi.org/10.1063/1.2909554>
- Kulatilaka WD, Lucht RP, Roy S, Gord JR, Settersten TB (2007) Detection of atomic hydrogen in flames using picosecond two-color two-photon-resonant six-wave-mixing spectroscopy. *Appl Opt* 46:3921–3927. <https://doi.org/10.1364/AO.46.003921>
- Kulatilaka WD, Hsu PS, Gord JR, Roy S (2011) Point and planar ultraviolet excitation/detection of OH-radical laser-induced fluorescence (LIF) through long optical fibers. *Opt Lett* 36:1818–1820. <https://doi.org/10.1364/OL.36.001818>
- Leschowski M, Dreier T, Schulz C (2014) An automated thermophoretic soot sampling device for laboratory-scale high-pressure flames. *Rev Sci Instr* 85:045103. <https://doi.org/10.1063/1.4868970>
- Leschowski M, Dreier T, Schulz C (2015) A standard burner for high pressure laminar premixed flames: detailed soot diagnostics. *Z Phys Chem* 229:781–805. <https://doi.org/10.1515/zpch-2014-0631>
- Luque J, Crosley DR, (1999) LIFBASE: Database and spectral simulation program (Version 1.5). SRI International Report MP
- Matynia A, Idir M, Molet J, Roche C, de Persis S, Pillier L (2012) Absolute OH concentration profiles measurements in high pressure counterflow flames by coupling LIF, PLIF, and absorption techniques. *Appl Phys B* 108:393–405. <https://doi.org/10.1007/s00340-012-4959-z>
- Meier W, Weigand P, Duan XR, Giezendanner-Thoben R (2007) Detailed characterization of the dynamics of thermoacoustic pulsations in a lean premixed swirl flame. *Combust Flame* 150:2–26. <https://doi.org/10.1016/j.combustflame.2007.04.002>
- Mohri K, Goers S, Schöler J, Rittler A, Dreier T, Schulz C, Kempf A (2017) Instantaneous 3D imaging of highly turbulent flames using computed tomography of chemiluminescence. *Appl Opt* 56:7385. <https://doi.org/10.1364/AO.56.007385>
- Mom AJA, Jansohn P (eds) (2013) *Modern Gas Turbine Systems, 1 - Introduction to gas turbines*, 1st edn. Woodhead Publishing, Philadelphia
- NIST Chemistry WebBook (2023), SRD 69 from <https://webbook.nist.gov/cgi/fluid.cgi?ID=C124389&Action=Page>
- Nori VN, Seitzman JM (2009) CH* chemiluminescence modeling for combustion diagnostics. *Proc Combust Inst* 32:895–903. <https://doi.org/10.1016/j.proci.2008.05.050>
- Parajuli P, Paschal TT, Turner MA, Wang Y, Petersen EL, Kulatilaka WD (2021) High-speed hydroxyl and methylidyne chemiluminescence imaging diagnostics in spherically expanding flames. *AIAA J* 59(8):3118–3126. <https://doi.org/10.2514/1.J060103>
- Parajuli P, Wang Y, Hay M, Katta VR, Kulatilaka WD (2022) Femtosecond two-photon LIF imaging of atomic hydrogen in high-pressure methane-air flames". *Proc Combust Inst.* <https://doi.org/10.1016/j.proci.2022.09.040>
- Paul PH (1994) A model for temperature-dependent collisional quenching of OH $A^2\Sigma^+$. *J Quant Spec and Radiat Trans* 51:511–524. [https://doi.org/10.1016/0022-4073\(94\)90150-3](https://doi.org/10.1016/0022-4073(94)90150-3)
- Roy S, Kulatilaka WD, Lucht RP, Glumac NG, Hub T (2002) Temperature profile measurements in the near-substrate region of low-pressure diamond-forming flames. *Combust Flame* 130:261–276. [https://doi.org/10.1016/S0010-2180\(02\)00379-6](https://doi.org/10.1016/S0010-2180(02)00379-6)

- Seitzman JM, Hanson RK (1993) Two-line planar fluorescence for temporally resolved temperature imaging in a reacting supersonic flow over a body. *Appl Phys B* 57:385–391. <https://doi.org/10.1007/BF00357380>
- Shaddix, CR (1999) Correcting thermocouple measurements for radiation loss: a critical review. 33rd ASME National Heat Transfer Conference, Albuquerque, New Mexico.
- Shaddix, CR. (2017). A new method to compute radiant correction of bare-wire thermocouples. 10th Mediterranean Combustion Symposium, Naples, Italy, September 17–21, 2017.
- Tobias J, Depperschmidt D, Welch C, Miller R, Iddi M, Agrawal AK, Daniel R Jr (2019) OH* chemiluminescence imaging of the combustion products from a methane-fueled rotating detonation engine. *J Eng Gas Turbines Power* 141:021021. <https://doi.org/10.1115/1.4041143>
- Tu X, Wang L, Qi X, Yan B, Mu J, Chen S (2020) Effects of temperature and pressure on OH laser-induced fluorescence exciting the A-X (1,0) transition at high pressures. *Chinese Phys B* 29:093301. <https://doi.org/10.1088/1674-1056/aba5ff>
- Wang Y, Jain A, Kulatilaka WD (2019a) Hydroxyl radical planar imaging in flames using femtosecond laser pulses. *Appl Phys B* 125:90. <https://doi.org/10.1007/s00340-019-7203-2>
- Wang Y, Taghizadeh S, Karichedu AS, Kulatilaka WD, Jarrahbashi D (2019b) Piloted liquid spray flames: a numerical and experimental study. *Combust Sci Technol* 192:1887–1909. <https://doi.org/10.1080/00102202.2019.1629431>
- Wang Y, Jain A, Schweizer C, Kulatilaka WD (2021) OH, PAH, and sooting imaging in piloted liquid-spray flames of diesel and diesel surrogate. *Combust Flame* 231:111479. <https://doi.org/10.1016/j.combustflame.2021.111479>
- Yin Z, Carter CD, Lempert WR (2014) Effects of signal corrections on measurements of temperature and OH concentrations using laser-induced fluorescence. *Appl Phys* 117:707–721. <https://doi.org/10.1007/s00340-014-5886-y>
- Zhao M, Buttsworth D, Choudhury R (2018) Experimental and numerical study of OH* chemiluminescence in hydrogen diffusion flames. *Combust Flame* 197:369–377. <https://doi.org/10.1016/j.combustflame.2018.08.019>

Publisher's Note Springer Nature remains neutral with regard to jurisdictional claims in published maps and institutional affiliations.

Springer Nature or its licensor (e.g. a society or other partner) holds exclusive rights to this article under a publishing agreement with the author(s) or other rightsholder(s); author self-archiving of the accepted manuscript version of this article is solely governed by the terms of such publishing agreement and applicable law.